Received: 20 March 2025 | Revised: 9 May 2025 | Accepted: 16 June 2025
DOI: 10.1002/esp.70119

RESEARCH ARTICLE

ESPL WILEY

Morphometry and spatio-temporal evolution of salt karren

Guillermo Pérez-Villar[1] | **Francisco Gutiérrez**[1] | **Alfonso Benito-Calvo**[2] | **Carles Roqué**[3]

[1]Departamento de Ciencias de la Tierra, Universidad de Zaragoza, Zaragoza, Spain

[2]Laboratorio de Cartografía Digital y Análisis 3D, Nacional de Investigación sobre Evolución Humana (CENIEH), Burgos, Spain

[3]Departamento de Ciencias Ambientales, Facultad de Ciencias, Universitat de Girona, Girona, Spain

Correspondence
Guillermo Pérez-Villar, Departamento de Ciencias de la Tierra
Universidad de Zaragoza, C/Pedro Cerbuna 12; 50009, Zaragoza, Spain.
Email: perezvillarguillermo@gmail.com

Funding information
Ministerio de Ciencia e Innovación, Grant/Award Number: PID2021-123189NB-I00; European Social Fund, Grant/Award Number: PRE2022-101600

Abstract

Morphometric data on karren developed in evaporite rocks, and especially salt, are almost lacking. Additionally, the models proposed to explain the evolution of some karren such as solution flutes (rillenkarren) and solution bevels are not based on real examples but on physical experiments or conceptual models poorly supported with data. Rocksalt, thanks to its high solubility and transport-controlled dissolution kinetics, offers the opportunity to investigate the morphological evolution of karren in short periods of time. This work uses high-resolution, multi-temporal 3D surface models generated by Structure from Motion (SfM) photogrammetry of a salt exposure in the Cardona salt diapir, NE Spain, to address the following issues: (1) morphometric characterisation of salt karren, (2) comparison with data from other lithologies and (3) morphological evolution of salt karren. Solution pits and solution flutes in salt tend to have significantly larger width and much larger depth than in carbonate rocks and gypsum. Solution flutes and solution bevels show complex evolutionary patterns that do not align with the commonly advocated parallel retreat and morphological persistence model. Instead, flutes can experience substantial morphological changes involving coalescence by the destruction of slim ridges and splitting caused by incision in the resulting broad flutes. The rillenkarren-bevel junction experiences a general downward and backward displacement, but locally can propagate forward by the development of intra-bevel flutes that merge with the rillenkarren slopes. Pedestals can grow vertically at rates as high as 5 cm/year.

KEYWORDS
chemical erosion, rainpits, rillenkarren, salt karst, solution bevels

1 | INTRODUCTION

Karren are the most widespread landforms in karst terrains, referring to a variety of small-scale sculpturing features carved in the surface of carbonate and evaporite rocks. They have important implications from the applied perspective, including autogenic aquifer recharge, sinkhole development, paleoenvironmental indicators, erosion gauges (e.g. pedestals), stone decay and geoheritage (Ginés et al., 2009; De Waele and Gutiérrez, 2022). Karrenfields may have outstanding aesthetic value, as revealed by the fact that they are the main natural value of a number of UNESCO World Heritage Sites (e.g. stone forests of Yunnan in the South China Karst; Bemaraha Tsingy of Madagascar) (Williams, 2011). There is great deal of publications addressing the morphometry of the most common bare karren types developed on exposed carbonate rocks (e.g. solution flutes). However, morphometric data on karren in evaporite rocks, and especially in rocksalt, are almost lacking.

Some karren types tend to occur spatially associated, forming karren assemblages with some genetic link (Bögli, 1960). A common karren assemblage found in rock outcrops include solution pits developed on the crest of rock protuberances that grade downwards along the flanking slopes into solution flutes and solution bevels. It is widely accepted that solution pits and solution flutes (rillenkarren) are essentially generated by dissolution caused by direct rainfall. Here, dissolution is caused by impinging raindrops directly interacting with the rock, rather than by diffusion through a boundary layer attached to the rock surface. The downslope transition from a fluted surface to a planar solution bevel is explained by a change in the dissolution mechanism. The flow depth increases downslope to reach a critical value for which raindrops do not have sufficient kinetic energy to penetrate the boundary layer, and dissolution is dominated by uniform sheetwash (Ginés & Lundberg, 2009; Glew & Ford, 1980; Lundberg & Ginés, 2009). Some authors indicate that biological and mechanical erosion can also play a significant role in the development of solution flutes (e.g. Fiol, Fornós, & Ginés, 1996; Mottershead, Moses, & Lucas, 2000). A number of publications address the morphological evolution of solution flutes, but the models and concepts proposed are based on physical experiments and conceptual models based on an ergodic assumption (i.e. substitution of space by time) or lacking an empirical basis (Lundberg & Ginés, 2009). Dunkerley (1979) suggested that solution flutes result from the connection of rows of small depressions. Glew and Ford (1980) reproduced the formation of solution flutes on plaster of Paris (artificial gypsum) and salt with variable inclinations (22.5–60°) exposed to constant rainfall. They observed the following morphological evolution: (1) rills with variable widths initiated in the crestal area and increased their width uniformity by a process of coalescence, (2) rills deepened and lengthened downslope maintaining a stable width and (3) rills reached maximum length grading downslope into a solution bevel; and (4) both the mature fluted and planar surfaces evolved by parallel retreat preserving their morphology. Mottershead, Moses and Lucas (2000) and Mottershead and Lucas (2004) proposed that greater erosion may occur in the fragile crest of the ridges, where mechanical erosion has greater contribution, implicitly challenging the parallel retreat and 'morphological persistence' model of Glew and Ford (1980).

Karren developed on rocksalt, thanks to its high solubility (356 g/l; mass of solute dissolved in 1 L of solvent), evolve very rapidly, offering an excellent opportunity to investigate morphological changes over short periods of time. This work characterises morphometrically various types of karren (solution pits, solution flutes, solution bevels and pedestal) developed on a salt exposure located in the Cardona diapir, NE Spain. The obtained parameters are compared with those published for carbonate rocks and gypsum. It also documents for the first time the evolution of natural karren using multi-temporal high-resolution 3D point clouds generated by Structure from Motion (SfM) photogrammetry (James et al., 2019). The accurately observed geomorphic changes are compared with evolutionary models proposed by other authors based on physical experiments and conceptual models.

2 | GEOLOGICAL AND GEOMORPHOLOGICAL SETTING

2.1 | General setting of the Cardona diapir

The emergent Cardona salt diapir is located in the northeastern sector of the Ebro Cenozoic Basin in NE Spain (Figure 1). The sedimentary fill in this sector of the foreland basin consists of a succession of folded Paleogene formations that record a general regressive evolution. The late Eocene Cardona Saline Formation is a marine evaporitic unit with an initial thickness of around 300–350 m, mainly consisting of halite and including a significant proportion of K-Mg chlorides (Pueyo, 1975; Riba, Reguant, & Villena, 1983; Rosell & Pueyo, 1997). The Cardona Saline Formation is conformably overlain by the late Eocene–Oligocene Suria and Solsona formations, forming a succession several hundred meters thick dominated by an alternation of mudstones and sandstones deposited in alluvial environments. These Paleogene sediments are affected by buckle folds detached along the Cardona Saline Formation, which shows significant thickening in the anticline cores (Sans, 2003; Sans & Verges, 1995). The Cardona salt extrusion occurs

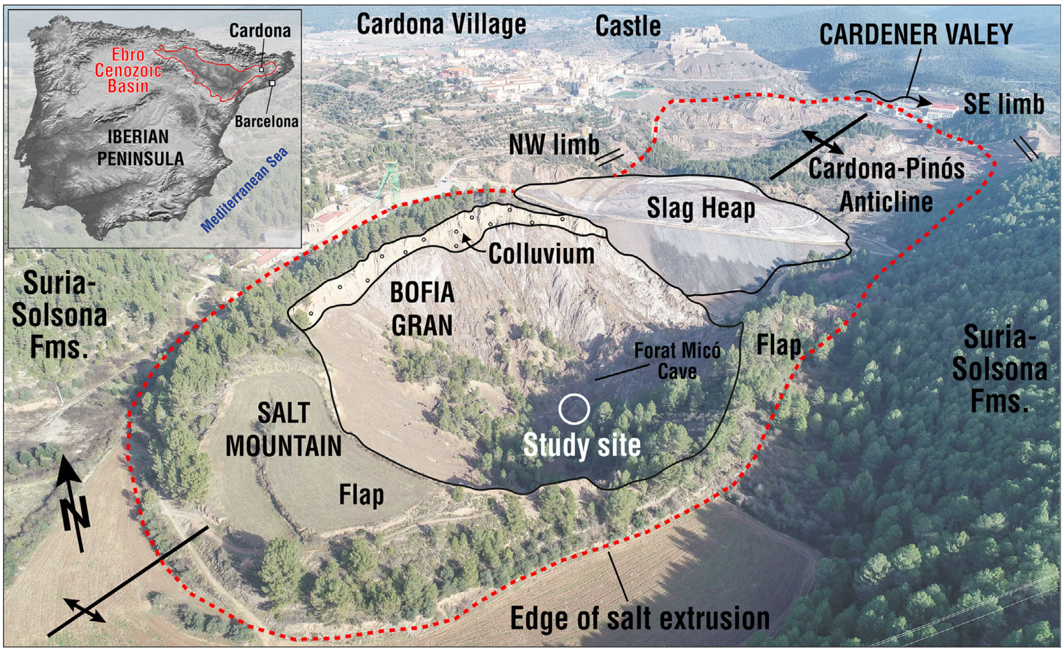

FIGURE 1 Geographic and geological setting of the active Cardona salt extrusion. The inset map depicts the location of the Cardona Diapir in the NE sector of the Ebro Cenozoic Basin. The annotated image shows the Cardona salt extrusion associated with the Cardona-Pinós anticline and the transverse Cardener River valley. The study site is situated in the bottom of the Bofia Gran, a large internally drained depression carved in the dome-shaped Salt Mountain, largely covered by upturned colluvial flaps.

in the core of the NE–SW-trending Cardona-Pinós Anticline and spatially associated with the SE-flowing Cardener River (Riba, Ramírez del Pozo, & Maldonado, 1975). This transverse drainage has excavated a deeply entrenched valley that cut across the folding structure (Figure 1).

The post-shortening emergence of the salt at Cardona was initiated in Late Quaternary times by the unroofing of the crest of the salt-cored Cardona-Pinós Anticline, related to the entrenchment of the discordant Cardener River. The breaching of the overburden by fluvial erosion led to the break out and spelling of the salt, forming an actively rising salt extrusion (passive salt wall) that has expanded progressively to the SW on the southern margin of the Cardener River (Figure 1). The currently active salt rise is driven by the combined effect of two differential loading mechanisms (Pérez-Villar et al., 2024): (1) greater load in the synclines than in the anticlines, where supra-salt sediments are much thicker (overburden loading), and (2) greater load at the valley margins than in the valley floor (erosional unloading). The salt tends to flow laterally and vertically towards areas subject to lower load: the anticline core and the unloaded valley floor.

Active diapirism at Cardona, a historically important salt mining site, was already reported in Roman times. The writer Aulo Gelio (125–180 AD), in his book Noctes Atticae (book II, chapter XXII), indicated ‘fodinae pulcherrimae mons ex sale mero magnus: quantum demas, tantum acrescit’, meaning ‘an enormous mountain of pure salt, the more you extract, the more it grows’. Rates of diapiric salt rise has been assessed by geological and geodetic methods. Raised Late Holocene strath terraces carved in salt bedrock and dated by radiocarbon indicate long-term uplift rates within the range 36.5–12.2 mm/yr. The vertical displacement rates show an increase towards the axis of the salt wall, away from the frictional forces that operate at the margins (Pérez-Villar et al., 2024). Similar vertical displacement rates and spatial patterns have been obtained by DInSAR studies, including the decomposition of vertical and horizontal displacement (Pérez-Villar et al., 2025). The data of current surface change reveal that in salt exposures, the continuous surface halokinetic uplift can be reduced or even overwhelmed by dissolutional erosion; the net surface change results from rock uplift minus surface erosion. DInSAR data indicate net vertical surface uplift in the salt exposures associated with the investigation site of this work (floor of the Bofia Gran) of around 0.5–1.5 cm/yr (Pérez-Villar et al., 2025) (Figure 1).

The NE–SW-oriented Cardona salt extrusion is 2-km long, 0.7-km wide and covers around 0.9 km^2. In its SW sector, where the salt has emerged more recently (i.e. immature landscape), it shows a dome-shaped protruding hill (the Salt Mountain) with a maximum local relief of 90 m (Figure 1). On the outer slopes of the hill, the salt is covered by flaps of upturned (i.e. drape folded) Quaternary deposits mainly made up of bouldery and gravelly colluvial facies that inhibit dissolution. In the central sector, the hill is carved by a funnel-shaped karst depression 300-m long and 70-m deep (the Bofia Gran) (Lucha et al., 2008; Pérez-Villar et al., 2024). This basin displays steep salt slopes dissected by gullies and sculptured by ubiquitous karren, forming striking karrenfields. These salt slopes are locally mantled by gravelly colluvial deposits derived from the uplifted colluvial flaps capping the salt at the rim of the depression (Figure 1). The Bofia Gran is drained by a short NE-directed bedrock channel with multiple notches that disappears in a swallow hole. This sink is the upper entrance of the 640-m long Forat Micó Cave (Cardona & Viver, 2002), characterised by a highly sinuous canyon with multiple tiered notches and hanging meanders developed under vadose conditions in rapidly rising salt bedrock. The investigation site selected in this work corresponds to salt slopes in the bottom of the Bofia Gran that exhibit a significant diversity of karren types.

2.2 | The investigation site

The selected salt outcrop, covering around 25 m^2, is located in the axial sector of the Cardona salt wall and in the bottom of the Bofia Gran karst depression (Figure 1). Here, the Late Eocene Cardona Saline Formation consists of halite beds with dominant centimetre-scale thickness, separated by millimetre-thick partings of grey clay (Figure 2). The halite layers and the clay partings represent around 93% and 7% of the rock mass, respectively (Figure 3a). The interbedded clay includes some gypsum, and X-Ray analyses of the clay fraction (<2 μm) on oriented aggregates indicate 81% of illite and 19% of chlorite. Two main salt packages can be differentiated on the basis of the colour of the halite beds: a stratigraphically lower one with orange halite and an upper one with grey, red and orange halite (Figure 2). The salt shows teardrop curtain folds with nearly vertical

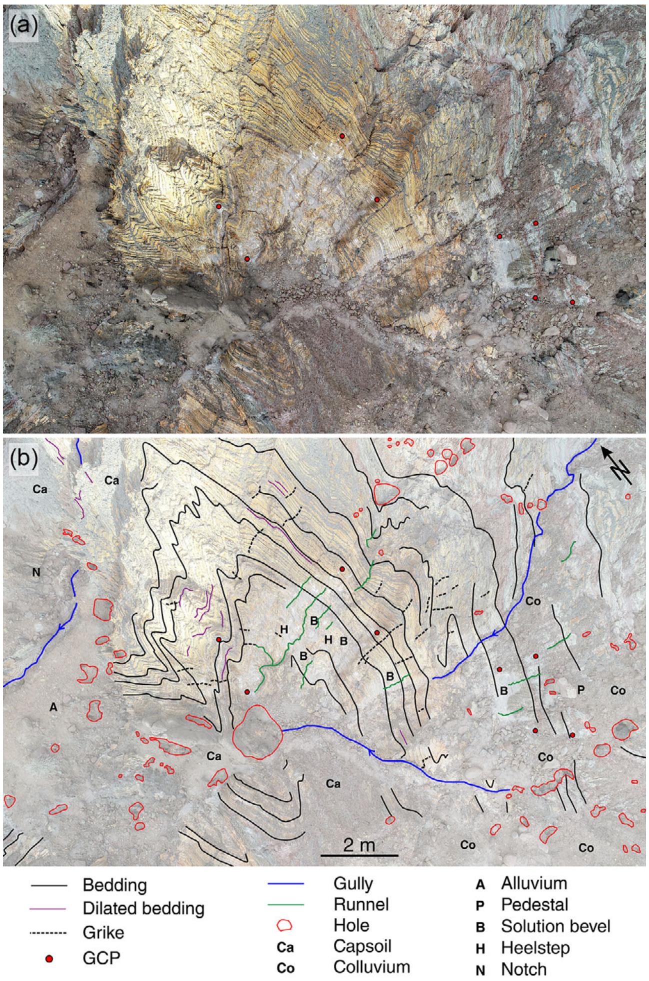

FIGURE 2 Annotated vertical image of the study site showing the distribution of ground control points, as well as the main structural and geomorphic features.

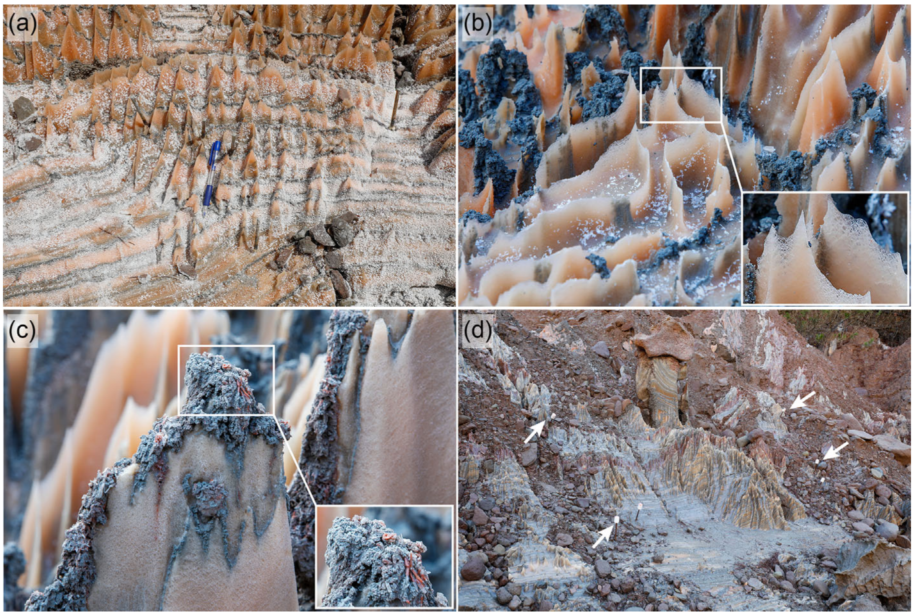

FIGURE 3 Images showing some of the weathering features and karren developed at the investigation site. (a) Thinly bedded orange halite with grey clay partings carved by transverse solution flutes and solution bevels coated by saline efflorescence of white halite crystals. Note the swelled clay in the upper left and local stony cover. (b) Close up view of open solution pits that connect with solution flutes, which edges are defined by extremely sharp (crystal thickness; inset) combs and spikes. Note the acicular halite crystals precipitated on the salt bedrock and expanded porous clay associated with the clay partings. (c) Salt ridge with expanded clay from clay parting showing high porosity and acicular reddish orange gypsum crystals (inset). (d) General view of the eastern sector of the site at the foot of salt slopes covered by colluvium and loose stones. The area shows a pedestal associated with a sandstone boulder and solution flutes that grade into solution bevels. Arrows point to ground control points.

axes. These steeply plunging folds develop where the diapiric salt flows upwards into a constriction (e.g. diapir stem) experiencing radial contraction (Jackson & Hudec, 2017; Talbot & Jackson, 1987). The main curtain fold at the site has a dominant N–S orientation in plan view and displays both disharmonic and similar (i.e. bed thickening in the hinges) geometries typical of plastic flow structures. The variable slope direction at the study site tend to be oriented perpendicularly to the strike of the bedding and towards the core of the involuted curtain fold. This implies that runoff as well as the orientation and slope of the resulting karren (e.g. flutes, bevels and runnels) tend to be oriented perpendicularly to the stratification, cutting across bedding (Figure 2). The salt bedrock locally shows some joints that may have been widened by dissolution to form rectilinear grikes (*Kluftkarren*) of decimetre- to metre-scale length, either air filled or clay filled. The joints and grikes essentially occur in the fold limbs as observed in the map view, and tend to have a bedding-normal E–W trend.

The surface of the salt can be locally covered by rather continuous efflorescences of white fibrous halite, according to X-ray analyses (Figure 3a, b). These crystals result from the following sequence of processes: (1) condensation of water on the rock surface forming appreciable water drops or films, (2) dissolution of halite by the strongly infra-saturated condensation water, and (3) evaporative salt precipitation driven by factors such as insolation and/or temperature rise. These condensation–dissolution and re-precipitation cycles can play a considerable preparatory role on salt erosion, in as much as the halite efflorescences can be readily detached and dissolved at the onset of rainfall events. The clay partings are locally expressed at the surface as protruding masses of highly porous clay with bulbous or glomerular morphologies and eye-visible acicular gypsum crystals (Figure 3b, c). Considering the lack of swelling clay minerals (e.g. smectite), the expansion of the weathered clay can be attributed to a porosity increase associated with wetting and drying cycles, accompanied by dissolution and re-precipitation of displacive gypsum crystals. The selective removal of salt as solute by dissolutional erosion leads to the in situ accumulation of clay on low gradient surfaces, eventually forming continuous mantles of residual clay. This non-consolidated regolith that functions as a protective cover that decelerates dissolutional denudation in diapirs is known as capsoil (Bruthans et al., 2009; Zarei, Raeisi, & Talbot, 2012) (Figure 2). Significant dilation can be locally observed along clay partings, specially ridges and protuberances where the rising and de-stressed bedrock has been laterally unconfined. These near-surface permeability features together with the grikes are responsible for the permeable epikarst in salt extrusions, which rapidly grade downwards into impermeable salt bedrock where viscous flow tends to anneal any discontinuity (De Waele & Gutiérrez, 2022; Talbot & Pohjola, 2009; Zarei, Raeisi, & Talbot, 2012).

The salt slopes lying above the investigation site are partially mantled by loose to poorly consolidated gravelly colluvial deposits derived for the retreating rim of the Bofia Gran, capped by the upturned colluvial flaps (Figures 1 and 2). Reworked clasts accumulate on low and irregular surfaces and tend to concentrate in gullies and runnels. Large boulders can protect the underlying salt rock from dissolution, leading to the development of pedestals (*Karrentische* or table karren; Bögli, 1961) with salt stems several decimetres high, like the one located in the eastern sector of the study site (Figure 3d). The morphology of the salt slopes at the site are dominated by a characteristic karren assemblage (De Waele & Gutiérrez, 2022) comprising tightly packed solution flutes (rillenkarren) in the upper and steeper slope sections that give way to solution bevels (ausgleichsflächen) in the lower parts of the slopes (Figures 2 and 3). The rill–bevel junction is typically defined by a sharp change in slope, and some bevels display well-defined slope changes and steps. The low-gradient crest of the fluted slopes and humps often display a peculiar type of open rainpits (solution pits) that connect with solution flutes (Figure 3b). Both the fluted and bevelled slope sections are locally carved by slightly sinuous solution runnels (*Rinnenkarren*) and decantation runnels, the latter fed by conduits or gravel mantles (Figure 2). Some heelprints (*Trittkarren*) with tightly curved backscarps also occur on solution bevels. Numerous holes can be identified, mainly in areas with low and moderate gradient. They may correspond to nearly vertical solution conduits on exposed salt, and to small cover collapse sinkholes underlain by the former feature. These depressions function as runoff and sediment sinks. In fact, all the surface runoff of the investigation site infiltrates in a sinkhole-conduit associated with the core of the curtain fold (Figure 2).

3 | METHODOLOGY

SfM photogrammetry, together with field measurements, has been applied for the morphometric characterisation of various types of salt karren (solution flutes, solution bevels and solution pits) and to quantitatively assess geomorphic change in the karren features.

3.1 | SfM photogrammetry

High-resolution close-range SfM photogrammetry models were generated observing the guidelines indicated in James et al. (2019), using oblique overlapping photographs (.jpeg format) taken with a camera mounted on a tripod, with observation distances ranging from 1.5 to 5 m (Figure 4). A full-frame Canon EOS 5D Mark IV camera (CMOS sensor of 30.4 MP) and Canon 16–35 mm lens (f/4 L IS USM) fixed at 35 mm focal depth was used. To assure the acquisition of good quality images (i.e. exposure, focus), the camera parameters were set at high aperture values (f/8–11; high depth of field), low sensitivity (ISO 100–200; low noise) and automatic shutter speed. A total of five photographic surveys were conducted, covering a total time span of 715 days or 1.96 years (19 May 2021; 14 December 2021; 17 June 2022; 31 November 2022; 04 May 2023). The images of each survey, ranging from 38 to 73, were processed using the software Agisoft Metashape Professional 1.7.1© to produce high-density point clouds. The photogrammetric point clouds were referenced using the local coordinates of four targets (ground control points) placed on drilled erosion pins. The local coordinates were extracted from a TLS point cloud, in order to have a common referencing for further investigations (Figure 4). The spatial resolution of the point clouds ranges from 511 to 859 points/cm^2 and the error of the control points from 1.68 to 7.39 mm, increasing towards the younger models. The accuracy in the areas of interest of the models was assessed comparing the coordinates of stable points (e.g. sandstone clasts) in successive point clouds, with deviations <2 mm, significantly smaller than the erosional surface changes. This time-dependent decrease in the accuracy of the models could be attributed to differential displacement among the targets placed on diapirically rising salt and the potential distortion of the erosion pins on which the targets were inserted. The dense point clouds have an average of 269,316,022 points, a mean point density

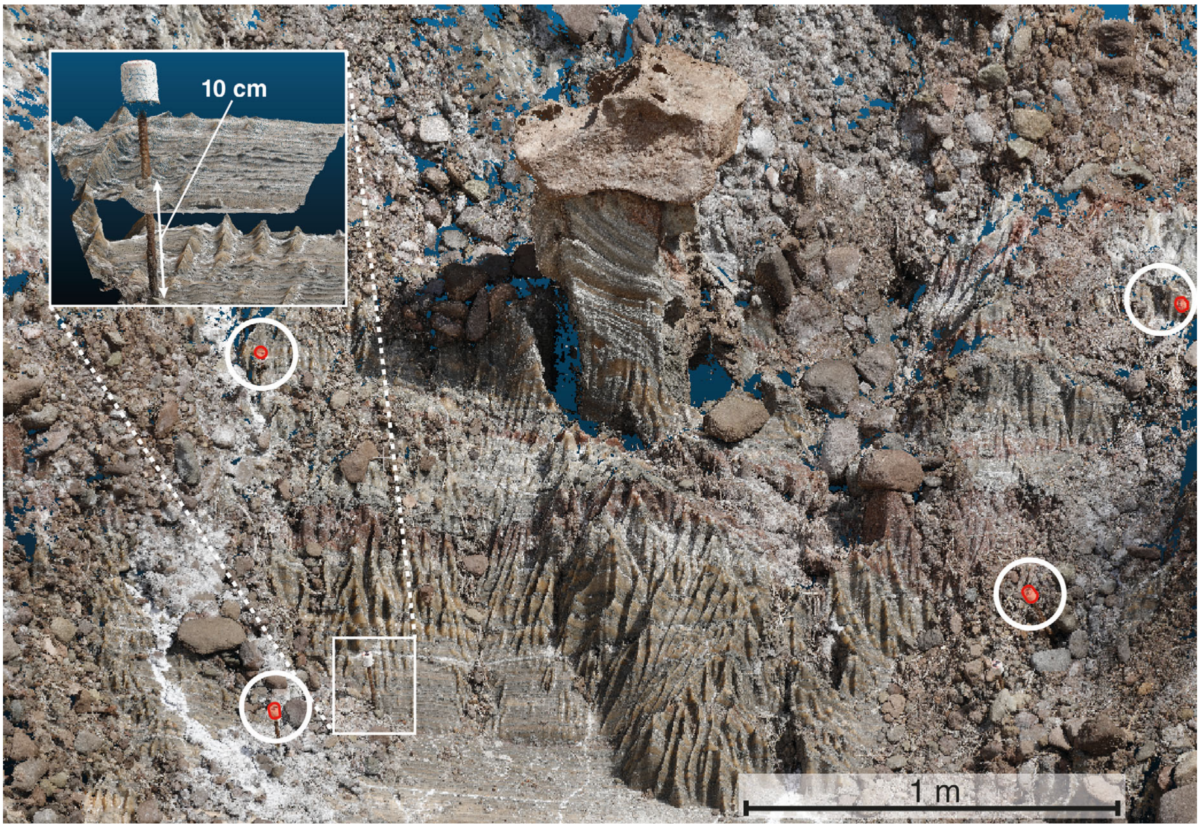

FIGURE 4 Texturised dense point cloud of the study area generated by ground-based photogrammetry (04 May 2023). Circles indicate ground control points placed on erosion pins used for referencing the models. Inset shows the superposition of two point clouds from different dates (19 May 2021 and 04 May 2023) captured from CloudCompare.

TABLE 1 Data of the photogrammetric 3D point clouds.

Date	19/05/21	14/12/21	17/06/22	31/11/22	04/05/23	Mean
Time lapse (days)	110	209	185	63	154	137.5
Number of points	2.4E+08	2.9E+08	2.9E+08	2.4E+08	2.30E+08	2.64E+08
Spatial resolution (points per cm^2)	511	650	696	859	686	741
Control points RMSE (mm)	1.685	3.053	5.108	7.387	6.835	4.626

Note: RMSE: root mean square error. Dates are presented as day/month/year.

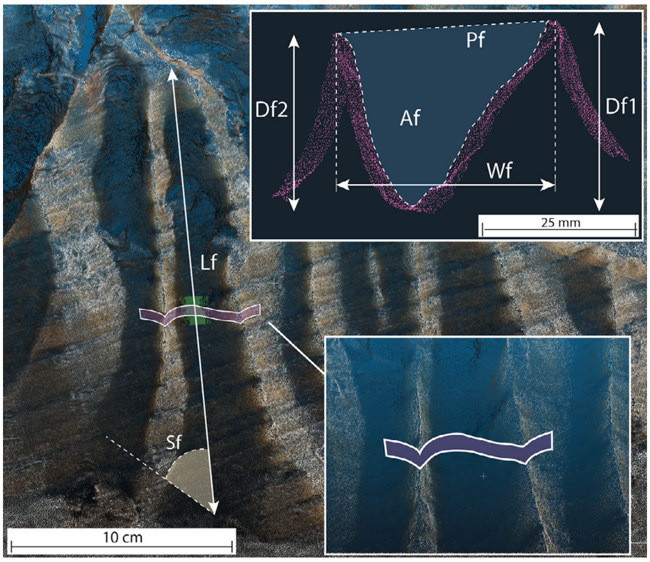

FIGURE 5 Excerpts from a 3D point could be generated by photogrammetry showing some of the morphometric parameters measured in solution flutes. The inset in the upper right corner shows a view of the middle sector of a flute perpendicular to the trough axis. See meaning of labels in Table 2.

of 741 points/cm^2 and an average registration model error (root mean square error; RMSE) of the ground control points of 4.6 mm estimated by Agisoft Metashape Professional©. Table 1 presents some relevant data on the photogrammetric surveys and the derived 3D dense point clouds.

3.2 | Morphometric measurements

Morphometric parameters have been measured in three types of salt karren: solution flutes (38), solution bevels (12) and solution pits (46). The parameters of the solution flutes and solution bevels were derived from high-resolution (ca. 6 points/mm^2) photogrammetric point clouds (Figure 5), while those of the solution pits were measured in the field with a digital calliper (Vernier Caliper Silverline, accuracy 0.01 mm). CloudCompare and AutoCAD© were used to measure the parameters from the 3D point clouds. Longitudinal profiles of the solution flutes were generated with Agisoft Metashape Professional©. Table 2 indicates the morphometric parameters measured for the different karren types, their definition and the measurement approach.

4 | KARREN MORPHOMETRY AND EVOLUTION

4.1 | Solution pits

Solution pits or rainpits are relatively scarce in the studied salt outcrop and mostly occur in low-gradient zones located at the crest of rock protuberances (e.g. broad crest of ridges and bosses), where the run-off contributing area is very limited and water–rock interaction is dominated by direct rainfall. The observed hollows smoothly cut across clay partings. The surrounding ridge in a great proportion of the solution pits has been breached, but they typically display concave bottoms capable of holding water and converging edges defined by razor-sharp crests with cusps and combs. Interestingly, their plan form shows some peculiarities that are rarely observed in rainpits developed on carbonate rocks (Ginés & Lundberg, 2009 and references therein) (Figure 6): (1) Frequent irregular shapes deviated from a simple subcircular geometry. (2) The sidewall of most of the measured pits has been breached, showing an opening typically connected to a solution flute. A few fully closed solution pits have been observed, but are very rare, indicating that the walls of the hollows are rapidly breached by dissolution. (3) Presence of relatively common elongated hollows with complex forms resulting from the coalescence of two or more adjoining rainpits. The criteria use to differentiated solution pits from the head of solution flutes include (Figure 6): (1) solution flutes have parallel flanking ridges, while the surrounding ridges of open solution pits display an almost complete enclosed geometry with converging walls at the narrow openings; (2) the trough axes of solution flutes have a sloping, continuously descending, and graded longitudinal profile, while the floor of solution pits is either concave, with a threshold associated with the opening, or planar and subhorizontal.

The major axis of the 46 measured solution pits have an average value of 32.0 mm, ranging between 55.93 and 17.54 mm (Table 3). The minor axis varies between 39.19 and 14.01 mm, with a mean value of 24.14 mm. The rainpits tend to be elongated, with maximum, minimum and average elongation ratios (i.e. major axis/minor axis) of 2.43, 1.01, and 1.33, respectively. The maximum and average depth of the pits are 110.65 and 42.99 mm, respectively. The rainpits are mostly deeper than long, with maximum, minimum and average depth to length (major axis) ratios of 3.73, 0.54 and 1.38, respectively. The width of the measured openings varies between 4.46 and 19.72 mm, with a mean value of 13.8 mm, which is 2.3 times smaller than the average major axis. The openings tend to occur on the long side of the elongated pits and connect to solution flutes downslope showing a similar parabolic cross profile.

TABLE 2 Morphometric parameters measured for solution flutes, solution bevels and solution pits and their definition and measurement procedure.

Parameter	Code	Definition	Procedure
Solution flutes			
Length	Lf	Length of the straight line between the uppermost and lowermost points of the flute axis (thalweg)	CloudCompare using 3D coordinates of the uppermost and lowermost points of the flute axis
Slope	Sf	Overall slope of the flute given by the straight line between the uppermost and lowermost points of the flute axis	Same as above
Width	Wf	Width between ridges measured on cross profiles perpendicular to the trough axis in the middle of the flute	Extraction from the point cloud of a section perpendicular to the trough axis in the middle of the flute (.dxf file) and measurement with AutoCAD©
Depth	Df1 Df2 Df	Distances between the crest of the ridges and the flute axis measured as a straight line perpendicular to the trough axis (major and minor depth; Df1, Df2) and the average (Df)	Same as above
Area	Af	Cross-sectional area perpendicular to the trough axis in the middle of the flute	Same as above
Perimeter	Pf	Length of the cross profile of the flute perpendicular to the trough axis plus the length of the line between the crests	Same as above
Solution bevels			
Length	Lb	Maximum 3D length of the bevel measured in the slope direction	CloudCompare using 3D coordinates of the uppermost and lowermost points
Slope	Sb	Slope of the planar surface	Same as above
Solution pits			
Major axis	MAp	Planimetric distance between the most distant points of the perimeter of the pit	Digital calliper
Minor axis	mAp	Planimetric length of the axis perpendicular to the major axis at its medial point	Digital calliper
Depth	Dp	Vertical distance between deepest point and the highest point of the pit perimeter	Digital calliper
Opening width	Op	Planimetric distance between the ridges at the pit opening	Digital calliper

Note: The definition of the morphometric parameters is inspired by Glew and Ford (1980), Palmeri, Madonia and Ferro (2020), Ginés and Lundberg (2009) and Lundberg & Ginés (2009).

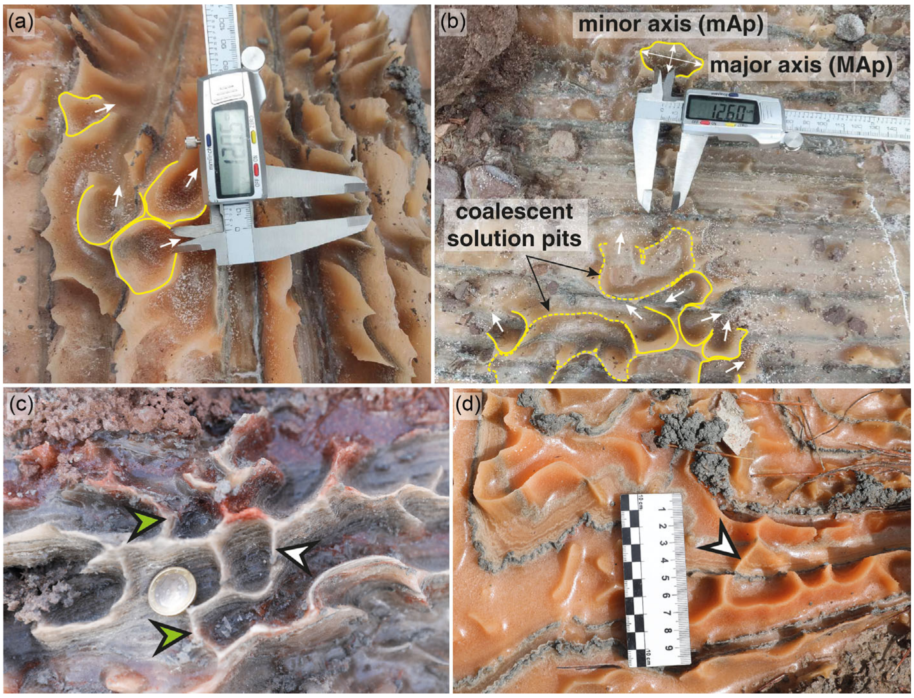

FIGURE 6 Examples of open and closed solution pits with irregular geometries in plan. Note that the pits smoothly cut across bedding and clay partings. (a) Open rainpits (yellow line) connected to solution flutes. (b) Coalescent pits (dashed yellow line). The openings are indicated by an arrow. The digital calliper in Figure 6a and b is placed to measure the width of the openings. (c) Closed solution pit (white arrow) and rainpits with breached ridges but enclosed bottom (green arrows). Coin 2.3 cm in diameter for scale. (d) Closed triangular-shaped rainpit.

TABLE 3 Summary statistics of the morphometric parameters of the analysed salt karren, indicating the number of features measured in parenthesis.

	Maximum	Minimum	Average	Est. dev.	Median
Solution pits (46)					
Major axis (Map, mm)	55.93	17.54	32.0	8.66	31.6
Minor axis (mAp, mm)	39.19	14.01	24.14	4.54	23.91
Elongation ratio (Map/mAp)	2.43	1.01	1.33	0.31	1.22
Opening width (Op, mm)	19.72	4.46	13.8	3.72	14.26
Depth (Dp, mm)	110.65	13.98	42.99	17.79	39.57
Depth to length ratio (Dp/Map)	3.73	0.54	1.38	0.56	1.23
Solution flutes (38)					
Length (Lf, cm)	129.1	5.8	31.6	25.3	23.2
Slope (Sf, °)	83.2	30.7	57.8	13.9	55.1
Width (Wf, mm)	54	15	30	10	30
Major depth (Df1, mm)	59	6.7	22.7	10.6	24.5
Minor depth (Df2, mm)	56	6			18.5
Width to depth ratio ((Wf)/(Df1 + Df2/2))	2.68	0.83	1.45	0.43	1.31
Area (Af, cm^2)	18	1	5	3	4
Perimeter (Pf, mm)	191.6	38.2	90	32.1	85.6
Depth to half-width ratio ((Df1 + Df2/2)/(Wf/2))	2.41	0.75	1.49	0.41	1.53
Solution bevels (12)					
Length (Lb, cm)	76.5	9	38	20	34
Slope (Sb, °)	31.67	3	12.6	9.03	10

Note: The parameters of the rainpits were measured with a digital calliper, while those of the solution flutes and solution bevels were extracted from photogrammetric point clouds.

4.2 | Solution flutes and solution bevels

Solution flutes or rillenkarren are the dominant karren on bare rock slopes with inclinations greater than 30° (Figures 2–5). These are closely packed furrows with rather constant width along their length and parabolic cross profiles separated by razor-sharp ridges that may display irregularities such as cusps, spikes and combs. The flutes can be straight to slightly sinuous, they mostly head at the crest of the slopes and their lower termination is often associated with an abrupt slope change giving way to a gentler planar solution bevel. On concave slopes, the flutes often display a contributory pattern converging into deeper flutes or runnels. On convex slopes, the inter-rill ridges often bifurcate, resulting in a downslope increase in the number of flutes. On planar slopes, the flutes are dominantly parallel.

The length of the 38 measured fully-developed solution flutes ranges between 1291 and 58 mm, with an average of 316 mm (Table 3). The slope of the flutes varies between 83.2 and 30.7°, with an average value of 57.8°. The width of the furrows, measured on cross profiles perpendicular to the trough axis at its middle section (Figure 5), shows a wide range between 54 and 15 mm, with an average of 30 mm (Figure 7a). The depth values (both major and minor) measured in the axis-normal cross profiles range between 59 and 6 mm, with an average of 22.7 mm. The flutes tend to be around 1.5 times wider than deep; average width to depth ratio of 1.45 (Figure 7b). The ranges of the computed cross-sectional area and perimeter are 100–1800 mm^2 and 38–192 mm, with average values of 500 mm^2 and 90 mm, respectively. The depth to half-width ratio has an average value of 1.49, indicating a parabolic cross profile deeper than that of a semicircular profile, which would have a ratio of 1. The longitudinal profile of 29 flutes has been plotted along their thalwegs. Ten of them show concave geometry, nine convex, and ten concave–convex. Bivariate analyses have been performed with a number of morphometric parameters to elucidate whether there is any relationship between them. The variable slope does not show any significant relationship with length ($R^2 = 0.01$, p-value $= 0.605$), depth (Df) ($R^2 = 0.0001$, p-value $= 0.954$) or width ($R^2 = 0.0002$, p-value $= 0.938$). The variables length and depth show a slight relationship ($R^2 = 0.34$, p-value $= 0.199$), with greater depth in longer flutes. The only moderate correlation is observed between width and depth (average between major and minor depth) ($Wf = 0.7303Df + 0.0139$; $R^2 = 0.6$ and p-value $= 6.06E\text{-}6$), showing a direct relationship between both variables.

The evolution of solution flutes through time has been addressed by comparing sections extracted from the five photogrammetric models with common referencing, representing sequential changes occurred in cumulative time lapses of 209, 394, 493 and 715 days (from 19 May 2021 to 04 May 2023). Slices of millimetre-scale width and perpendicular to the flute axes were used to extract the multi-temporal profiles, thus showing slope-normal geomorphic change (Figure 8). A total of 11 representative solution flute sections (Figure 8a–k) were selected covering some geomorphic and evolutionary diversity: (a, e) sections close to the head of flutes; (b, c, d, f, g, h) sections at the medial sector of flutes; and (i, j, k) sections of flutes newly formed during the monitoring period, and in the case of j and k developed on planar solution bevels. All the profiles have been represented with a common scale with no vertical exaggeration, allowing

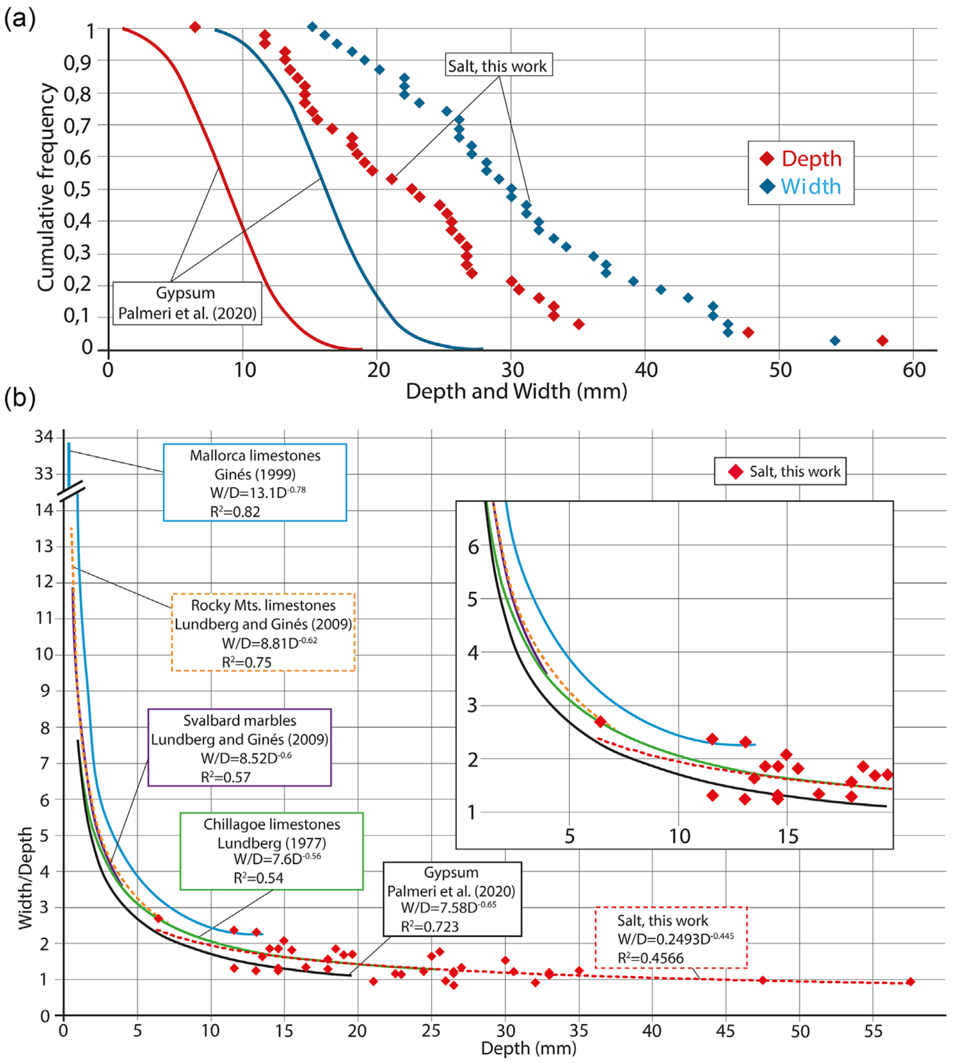

FIGURE 7 (a) Graph showing the cumulative frequency of the measured width (blue) and depth (red) in the studied solution flutes, together with curves depicting the size distributions reported for eight solution flutes in gypsum by Palmeri, Madonia and Ferro (2020). (b) Graph plotting width/depth ratio versus depth of solution flutes in the Cardona salt karst (red dashed line, this work), in gypsum arenite from Calabria, Italy (black solid line), in limestones at Chillagoe, Australia (green solid line), in marbles at Svalbard, Norway (purple solid line), in limestone in the Rocky Mountains, USA (orange dashed line), and in limestones in Mallorca Island, Spain (blue solid line). The source of the morphometric data, together with the regression equations and their coefficient of determination (R^2) are indicated in the inset squares.

the comparison of flutes among the different sections, with widths ranging from 16 mm (i) to 43 mm (e).

A number of works on rillenkarren suggest that flutes evolve by parallel slope-normal denudation, and consequently the troughs and the intervening ridges persist through time and tend to maintain their morphology once they have reached a mature stage (Glew & Ford, 1980; Lundberg & Ginés, 2009). This 'morphological persistence' pattern is only observed in sections c and f, where the flutes maintain their overall morphology and location, although the flanks may steepen resulting in the narrowing of the ridge. However, the most common evolution patterns observed involve complex changes in the cross-sectional geometry of the flutes, eventually leading to the development of new rills. In a number of cases, the ridges experience a progressive narrowing, while the bottom of the flutes broaden (b, e, g). Once the ridges attain a very slim and acute profile, they experience accelerated destruction (a, b, d). Eventually, the erosion of the ridge leads to the coalescence of two adjoining flutes to form a broad furrow with a relatively planar bottom (d, h). These wide troughs can be incised by rills, resulting in the developed of new nested flutes and/or the splitting of the furrow into two flutes with an intervening ridge (d, e, g, h, i). The sections initially located close to the head of rills associated with ridge bifurcations show a replacement of flutes by ridges (a, e). This geomorphic change is related to the downslope migration of the bifurcation point of the ridge (i.e. head of flute), involving the widening of the flanking flutes at the bifurcation zone. The cross-profile of flutes newly formed in solution bevels tend to be relatively shallow and narrow and show apparently haphazard phases of degradation (ridge attenuation or destruction) and rejuvenation (flute deepening and creation) (j, k).

The 12 solution bevels measured occur bellow rillenkarren, in most cases with an abrupt slope attenuation between the fluted and bevelled surfaces (i.e. rill extinction line). Solution bevels are typically wider than long, may display slope breaks and steps, and are locally incised by runnels, grikes, heelprints, and patches of solution flutes. The measured lengths range between 765 and 90 mm, with an average value of 380 mm. The slopes vary between 31.8° and 2°, with a

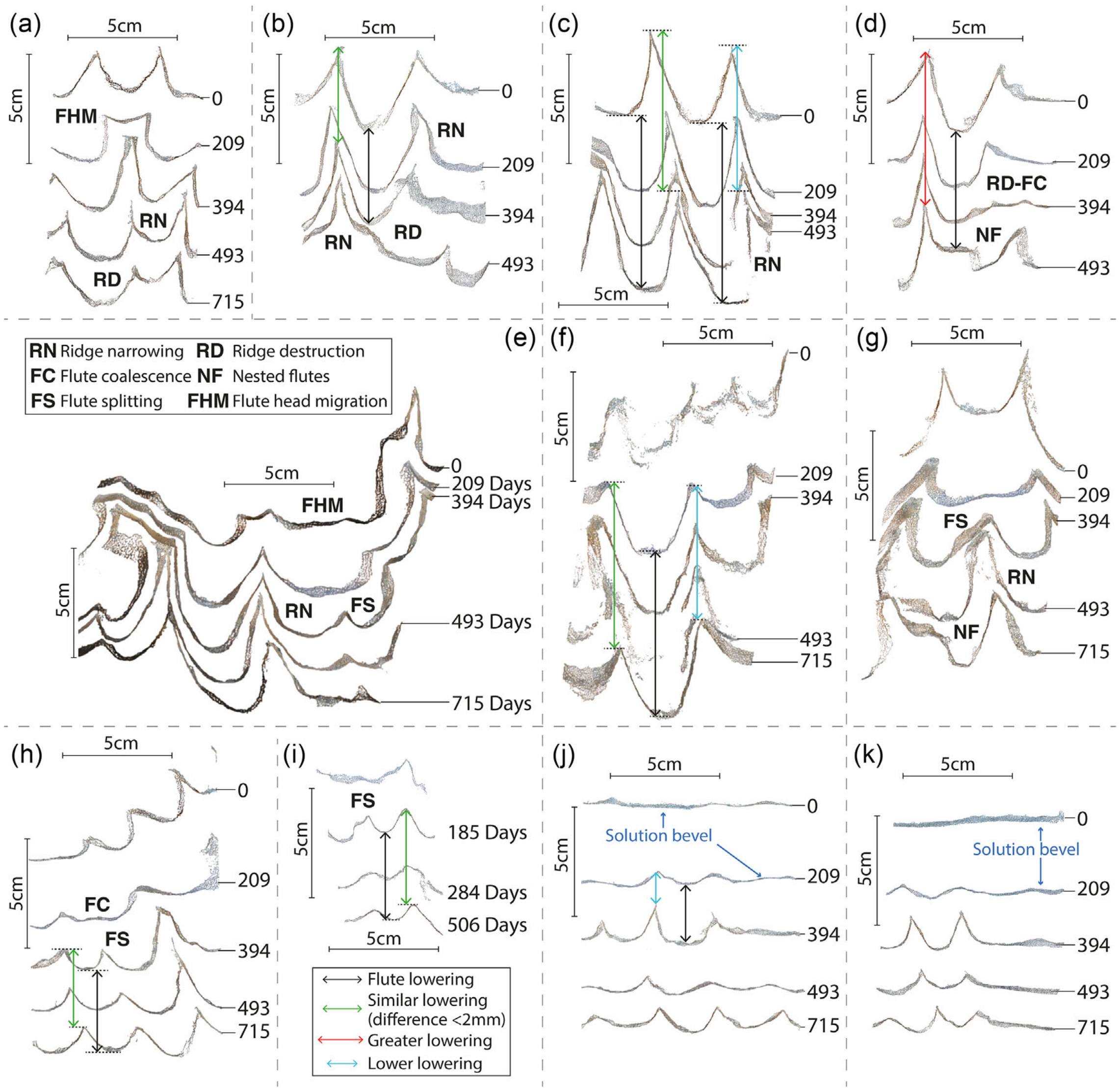

FIGURE 8 (a–k) Multi-temporal sections of flutes extracted by clipping the high-resolution photogrammetric point clouds (19 May 2021, 14 December 2021, 17 June 2022, 24 September 2022 and 04 May 2023) with slices of millimetre-scale width and perpendicular to the flute axes. Numbers indicate the time elapsed in days since the oldest section. Colour arrows indicate whether the slope normal lowering in the ridge is similar (<2 mm difference; green), greater (red) or lower (blue) than that in the adjacent rill (black). Main types of geomorphic change indicated with letters.

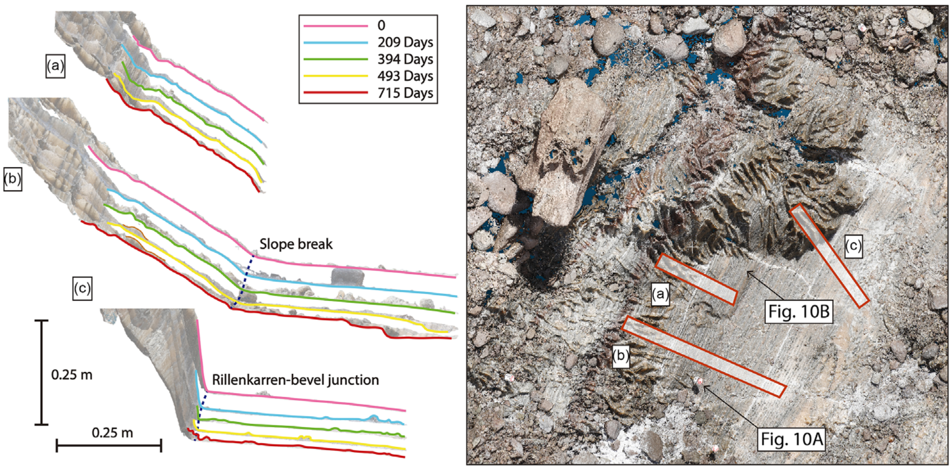

FIGURE 9 (a–c) Multi-temporal slope-parallel profiles of solution bevels extracted by clipping the high-resolution photogrammetric point clouds (19 May 2021, 14 December 2021, 17 June 2022, 24 November 2022 and 04 May 2023). Note that section b includes an intra-bevel slope break. Location of profiles is shown on the right. Numbers indicate the time elapsed in days since the first profile.

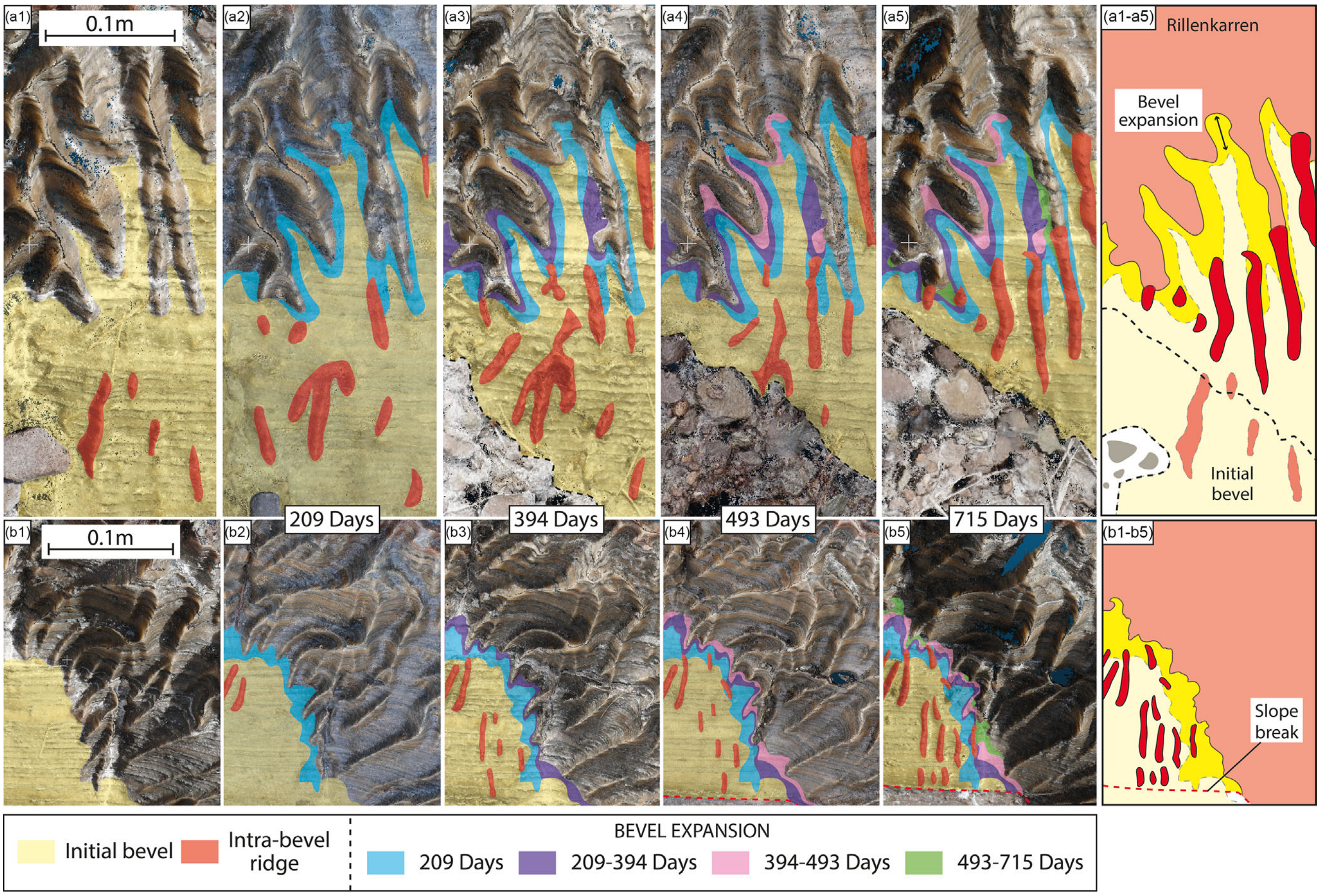

FIGURE 10 Multi-temporal and coincident zenithal views (photogrammetric dense point clouds) of rillenkarren and solution bevels showing the general backward retreat of the rillenkarren-bevel junction and the local development and expansion of solution flutes superimposed on the solution bevels. (a1–a5 and b1–b5) The main changes occurred between the first and the last monitoring date.

mean of 12.6° (Table 3). Figure 9 shows the evolution of the longitudinal profile of solution bevels and the lower part of the associated fluted slope at three locations, one of them including an intra-bevel slope break with a downslope gradient attenuation. Overall, the multi-temporal profiles reveal the following geomorphic changes: (1) parallel surface-normal lowering, which implies homogeneous denudation rate along the bevels and gradient persistence, (2) backward migration of the intra-bevel slope break that entails the expansion of the lower gentler bevel at the expense of the upper steeper bevel (Figure 9b) and (3) slow recession of the upslope edge of the bevels (i.e. rill extinction line; Figure 9a, c).

Figure 10 shows sequential zenithal images (dense point clouds) of two areas, providing a three-dimensional evolutionary picture that illustrates the progressive retreat of the rillenkarren-bevel junction and the development of solution flutes on solution bevels. The erosional lowering of the planar solution bevels is locally accompanied by the development of slope-parallel ridges (Figure 10a1, b2). The ridges expand longitudinally and eventually merge forming flutes in between (Figure 10a3, b3). Some expanding intra-bevel ridges connect with the ridges of the solution flutes in the rillenkarren slope, involving an abrupt expansion of the latter at the expense of the solution bevel (Figure 10a5, b4, b5). Overall, the rillenkarren-bevel junctions show a progressive backward retreat, resulting in the general expansion of the bevel, while locally the rilled area may increase by the superposition of flutes in the bevels, explained earlier.

4.3 | Salt pedestal

In the investigation site, there is a prominent salt pedestal capped by an elongated sandstone boulder with the major axis oriented perpendicular to the general slope gradient (Figure 4). Clasts tend to roll downslope with the *a*-axis oriented normal to the slope direction. The shielding boulder is around 60-cm long and 25-cm wide at the base. At the initial date of the monitoring period, the salt stem was 45-cm high, and its crown in contact with the boulder was 37-cm long and 24-cm wide. Thus, the boulder is larger than the top of the salt stem and forms overhangs. The nearly vertical walls of the stem change downwards into slopes carved by solution flutes forming a basal plinth. On both flanks of the pedestal, the salt stem is dissected by solutionally enlarged grikes that have evolved into holes separating small pinnacle-like spurs. Figure 11 illustrates the evolution of the longitudinal and transversal profile of the salt pedestal over a period of 715 days, showing the following features: (1) the contact between the boulder and the crown of the salt stem remained stationary; (2) the nearly vertical flanks of the salt stem situated right beneath the boulder were not affected by any appreciable retreat; (3) the medial-lower sections of the stem walls and the flutted slopes of the plinth show variable erosion that increases as the slope gradient decreases; (4) the junction between the stem walls and the rilled slopes of the plinth experienced a cumulative lowering of 10–11 cm, indicating the height increase of the pedestal over 1.96 years; (5) a major and abrupt

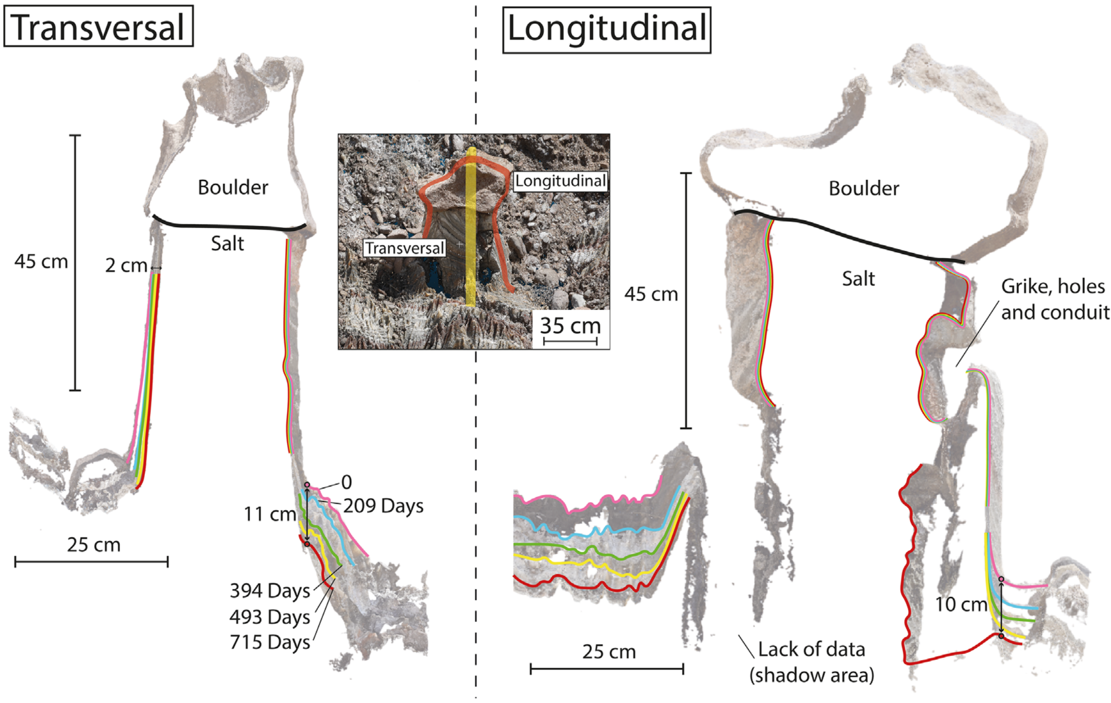

FIGURE 11 Multi-temporal transversal and longitudinal profiles derived from five photogrammetric point clouds showing the morphological evolution of the salt pedestal over a period of 1.96 years (751 days).

change is observed in one of the flanks of the salt stem between 493 and 715 days, when the pinnacle collapsed, resulting in a sudden local narrowing of the salt stem.

5 | DISCUSSION

5.1 | Solution pits

The review on rainpits by Ginés and Lundberg (2009) reveals that studies with morphometric data are very scarce and focussed on carbonate bedrock. The available reliable data are restricted to limestone outcrops in the Tramuntana Range of Mallorca Island, Spain (420-mm average precipitation) (Ginés, 1998; Ginés & Lundberg, 2009), and two rock types in Chillagoe, Australia (880 mm mean annual precipitation), namely fossiliferous reefal limestone and coarsely crystalline marble (Lundberg, 1977). The suitability of the data reported by Smith (1987) from southeast Morocco and by Zhang (1994) from Tibet remains uncertain, because the anomalously small dimensions of the karren, including pits in vertical walls, suggest that the features measured might not be actual rainpits (Ginés & Lundberg, 2009).

The studied rainpits in the Cardona salt karst show a number of peculiarities that differentiate them from those described in carbonate rocks, including their dominantly breached sidewalls, but mostly with concave floors, common elongated geometry, and frequent occurrence of compound pits resulting from the coalescence of adjacent single pits. The open status of the majority of the pits can be ascribed to the fast evolution of the hollows related to the highly solubility of the halite bedrock salt. Here, rainpits can form and grow very rapidly, eventually opening the perimeter by the recession and downwearing of the narrow enclosing edges. The breaching of the edge of the pits may lead to their connection with adjacent flutes (Dunkerley, 1979; Macaluso & Sauro, 1996) or to their coalescence with an adjoining pit. Although the majority of the measured pits are open, their morphometric parameters can be used to compare them with values from other areas, because the opening does not alter the computed parameters.

Rainpits in carbonate rocks tend to be nearly circular in plan form. In fact, the published works only provide one planimetric dimension (e.g. width, diameter). Proper characterisation of the pits in the Cardona salt karst, with a mean elongation ratio of 1.33, requires computing both major and minor axis. The studied rainpits have an average major axis of 32 mm, significantly larger than the mean diameters measured in the reefal limestone and marble of Chillagoe (20.9 and 16.2 mm), and the mean diameters of Mallorca (20.1 and 20.5 mm). The studied rainpits in salt are 2 to 1.5 times longer than those in carbonate rocks. The rainpits in Cardona, with an average depth of 42.99 mm, are 8 to 4.5 times deeper than those in Chillagoe (9.3 mm reefal limestone, 5.4 mm marble) and in Mallorca (10.4 mm). Moreover, the rainpits at Cardona show much higher depth to length ratio (1.23) than in the carbonate karsts of Chillagoe (0.44 reefal limestone, 0.33 marble) and Mallorca (0.5), indicating a greater vertical development. Overall, the presented data indicate that solution pits in salt rapidly lose their closed character, tend to be more elongated and larger (longer and deeper) than those in carbonate rocks, and attain a greater vertical development (higher depth to length ratio). All these differences can be largely ascribed to the high solubility and rapid transport-controlled dissolution kinetics of halite. Unfortunately, there is no morphometric data available from rainpits in gypsum to compare them with those developed on salt. The development of rainpits is essentially attributed to direct dissolution caused by impinging raindrops able to cut through water films. Dissolution by stagnant water and the removal of loose crystals and particles by splash erosion can also contribute to the enlargement of the pits. Rainpits in carbonate karsts areas are particularly abundant in semi-arid regions (Ginés & Lundberg, 2009). Ginés (1996), in an investigation on the distribution of rainpits and solution flutes in Mallorca, observed that the abundance of the former decreases with elevation up to an extinction level (500 m a.s.l., ca. 900 mm) from which solution flutes become dominant. The scarcity of rainpits and their dominantly open status at Cardona might be related to the local rainfall conditions, for which flute development is significantly more efficient and rainpits are rapidly integrated into flutes. Probably, rainpits could be more frequent under more arid conditions, a working hypothesis that could be tested investigating salt karren in other regions with lower rainfall (e.g. salt extrusions in the Zagros Mountains of Iran).

5.2 | Solution flutes and solution bevels

The only previous work that addresses the morphometry of solution flutes in salt bedrock was published by Mottershead, Moses and Lucas (2000). They measured flutes at three sites in the Cardona diapir with different rock types: (1) multicoloured halite beds with thin clay partings, designated as rocksalt; (2) halite made up of transparent glassy crystals up to 3 cm long apparently lacking impurities, designated as halite; and (3) pink fine-grained salt with putative K-Mg-chlorides, designated as carnallite. Morphometric data in Mottershead, Moses and Lucas (2000) are presented as median values (middle value) to avoid the effect of potential skewed distributions and the bias related to outliers. The median values reported from their 'rocksalt' site, with an evaporitic facies equivalent to that of our site, are relatively similar to our median values for width (24.72 vs. 30 mm), depth (13.9 vs. 21.5 mm) and width/depth ratio (1.82 vs. 1.31) (Table 3). The differences between the values could be related to difficult-to-assess factors, such as the texture of the salt layers, or the maturity of the selected flutes. In this work, all the measured features are fully developed flutes that extinguish at solution bevels.

Morphometric data from solution flutes developed in gypsum are also very scarce. Measurements carried out by Stenson and Ford (1993) in Nova Scotia, Canada (average precipitation 1100 to 2000 mm/yr) yielded mean width and depth values, and a mean width/depth ratio of 8 mm, 2.6 mm and 4.64, respectively. Measurements carried out by Mottershead, Moses and Lucas (2000) in gypsum at two sites in the United Kingdom and six sites in Spain yielded median values for width, depth and width/depth ratio of 9.9 mm, 3.2 mm, and 3.73, respectively, which are comparable with the means from Nova Scotia. Palmeri, Madonia and Ferro (2020) carried out multiple measurements along eight solution flutes carved in Messinian gypsarenite. Although they do not provide mean values, their graphs indicate average width and depth values of around 17 mm and 8 mm, respectively (Figure 7a). The comparison of the cumulative frequency distribution of their width and depth data with our measurements indicates persistent larger sizes and wider value ranges in salt (Figure 7a). Our width and depth values cover 0.55 and 0.94 orders of magnitude, respectively. The solution flutes analysed in this work are around 4–2 times wider, 10–3 times deeper and have significantly lower width/depth ratio than the limited available data for gypsum, suggesting that rillenkarren in salt tend to be much larger and may attain greater relative vertical development.

In contrast to evaporites, there is a wealth of morphometric data on solution flutes in carbonate rocks. Lundberg and Ginés (2009), in their comprehensive review on rillenkarren, compiled published (23 publications) and unpublished data from 50 locations ranging from arctic to tropical climates, of which 44 correspond to limestone, three to marble and three to dolomite. The mean morphometric values computed with their dataset (42 sites with average values) show notable differences with those of the solution flutes in salt investigated in this work. Our flutes are around two times wider (30 vs. 16.9 mm) and about 5 times deeper (22.7 vs. 4.4), resulting in a width/depth ratio three times lower (1.45 vs. 4.37). Mottershead (1996) described the longitudinal profile of solution flutes in limestones from Mallorca Island, Spain, concluding that flutes are characterised by a concave profile. The flutes analysed in this work display variable longitudinal profiles, including concave, convex and concave–convex.

A number of works on solution flutes in limestone report some correlation between different parameters. Mottershead (1996) found that flutes tend to be shallower on steeper slopes, but no such relationship is observed in our salt flutes (R^2 < 0.1). Some authors observed a moderate direct relationship between the slope and length of solution flutes (Crowther, 1998; Ford & Lundberg, 1987; Lundberg & Ginés, 2009). However, a number of studies (Dunkerley, 1979; Ginés, 1999), like in our case, document the lack of any significant relationship between those variables. There is a general direct relationship between the width and depth of solution flutes developed in carbonate rocks (Lundberg & Ginés, 2009). In the measured solution flutes of Cardona, such relationship can be described by the regression $Wf = 0.73Df + 0.0139$ ($R^2 = 0.6$). The coefficient 0.73 indicates that width tends to be around 70% the depth value. However, the regressions generated for solution flutes in limestone and marble show higher coefficients ranging from 0.92 to 2.67 (Lundberg & Ginés, 2009), indicating that in carbonate rocks, the flutes tend to have widths similar to or larger than their depths, and that solution flutes in salt tend to be deeper, as indicate the relatively low width to depth ratio computed in this work (1.45). Some authors suggest that the high-dissolution kinetics of halite may be the reason why rillenkarren in this lithology reach much greater depth than in gypsum and limestone (Lundberg & Ginés, 2009; Mottershead & Lucas, 2004).

Figure 7b shows the distribution of width/depth ratio versus depth reported for solution flutes developed in different lithologies and locations (Lundberg & Ginés, 2009 and references therein; Palmeri, Madonia, & Ferro, 2020). Some authors suggest that solution flutes in their initial evolutionary stages widen until the width stabilises, while the depth continues to increase (Glew & Ford, 1980; Mottershead & Lucas, 2001). Based on this concept, the graphs in Figure 7b could be considered to represent a morphometric evolutionary trend, from shallow immature flutes on the left to deeper and more mature flutes towards the right. The data from carbonate rocks show a tight depth range concentrated at 10–15 mm and reaching 25 mm, in contrast with the ample width/depth ratio, indicating that the width can be between 1.5 and 34 times larger than the depth. The best-fit curve for gypsum represents multiple measurements carried out along eight rills carved in gypsum arenite, suggesting a narrower width/depth range than in carbonate rocks (Palmeri, Madonia, & Ferro, 2020). In this case, the depth varies from ca. 2 to 18 mm, and the width/depth ratio indicates widths 1 to 7.5 times greater than the depth. However, these morphometric values may have limited

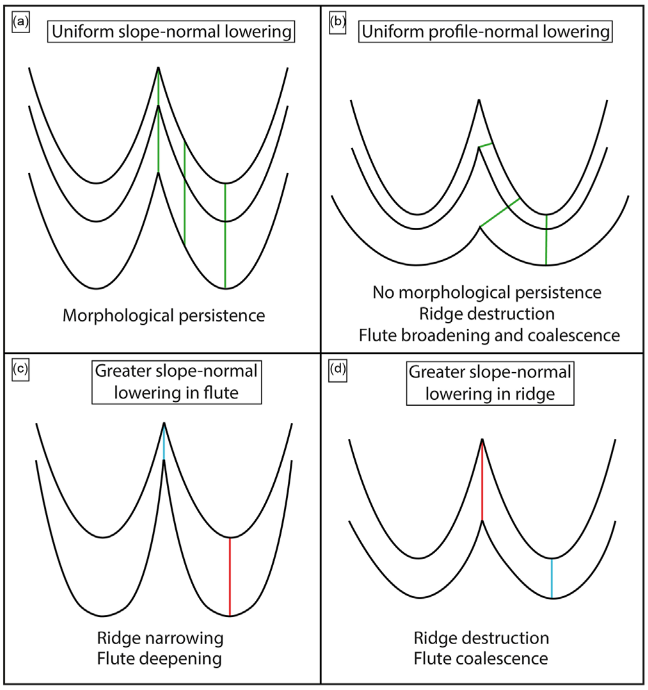

FIGURE 12 Theoretical models of flute evolution represented by slope-normal cross profiles, indicating the associated morphological changes. The models assume stationarity in the location of the ridges and flute axes. See explanation in the text.

representativeness, given the limited number of rills and the coarse-grained texture of the gypsum rock. Our data from salt show a very broad depth range covering one order of magnitude (6–59 mm), while the width/depth ratio is concentrated in a narrow range between 1 and 3, pointing to a rather constant proportionality between both parameters. Although the data from Cardona is probably biased by the site conditions and the selection of fully developed rills, they illustrate the large depth range and the high maximum depth of solution flutes in salt.

Figure 12 shows graphically four theoretical models of solution flute evolution considering slope-normal cross profiles and assuming stationarity in the location of ridges and flute axes. In model A, uniform slope-normal lowering across the flutes results in morphological persistence. This is the evolutionary model suggested for mature rillenkarren in a number of works (Glew & Ford, 1980; Lundberg & Ginés, 2009). In model B, featuring uniform profile-normal lowering, the evolution involves progressive ridge destruction and widening (i.e. interlimb angle) and eventually flute coalescence. Model C, representing greater slope-normal lowering in the flute, shows progressive ridge narrowing and steepening of the flute slopes and flute deepening. Model D, with greater slope-normal lowering in the ridge, entails ridge destruction and eventually flute coalescence. The sections analysed in this work illustrate that solution flutes in salt often experience complex evolution patterns in short periods of times (i.e. a single rainfall event), contributing to better understand the evolution of rillenkarren in salt. Cycles of flute coalescence and flute splitting are documented (Figure 8). At some stage, the ridges become progressively slimmer because of greater dissolution in the bottom of the flutes, following model C. Once the ridges reach a critical narrow width, they can experience accelerated destruction, as in model D. Enhanced erosion at these narrow ridges can be attributed to the very high surface/volume ratio (specific surface) facilitating rapid dissolutional erosion, and probably also greater contribution of mechanical erosion of a more fragile ridge. The obliteration of a narrow ridge leads to flute coalescence and the development of broad furrows, where new nested flutes and ridges can develop, starting a new cycle. The frequently advocated morphological persistence model (Figure 12a model) has been also observed in some sections at the temporal scale of our investigation (Figure 8c, f), but these flutes might experience substantial geomorphic changes at some stage, given the high solubility of salt and the highly dynamic nature of salt karren. Our data also show the downslope migration of the head of flutes situated below ridge bifurcations, probably related to enhanced dissolution at flute deflections and/or constrictions, where the increase in flow rate and turbulence contributes to increase dissolution rate.

The solution bevels documented in carbonate rocks and gypsum typically occur below surfaces fluted by rillenkarren without showing any significant slope change at the rill extinction level (Lundberg & Ginés, 2009 and references therein). However, the investigated bevels in salt mostly show a slope break at the rillenkarren-bevel junction, with gentler slope in the bevel. Integration of the data derived from the multi-temporal profiles (Figure 9) and the time-lapse zenithal images (Figure 10) reveal the following evolution patterns: (1) The bevels experience uniform slope-normal lowering (parallel profiles). This feature indicates that sheetwash maintains its dissolutional capability along the bevels, which is reasonable given the high solubility of halite and the short previous interaction of the rainfall water with the rock at the rillenkarren surface. (2) The rillenkarren-bevel junction experiences a general backward retreat involving the expansion of the bevel at the expense of the rillenkarren. Lundberg (2013) suggested that solution bevels evolve like pediments by the backward retreat of their upslope edge (i.e. backwearing, pedimentation). Our data indicate that downwearing is the dominant process, but there is also some backwearing and substitution of solution flutes by the bevelled surface (Figure 10). Complex patterns are also observed in solution bevels, involving the formation, growth and merging of ridges, leading to local superimposed solution flutes, that eventually may connect with the solution flutes of the rillenkarren surface (Figure 10). A similar evolution pattern has been documented on physical analogue models of solution flute development on plaster of Paris (Glew & Ford, 1980; Slabe, Hada, & Knez, 2016). The point clouds reveal that the inception of some ridges and flutes on the solution bevels is controlled by surface irregularities (e.g. protruding insoluble, particles) that distort the sheetwash (flow separation or convergence) and induce differential dissolution. The cross profile of these intra-bevel flutes shows phases of degradation and rejuvenation (Figure 8j, k). Further investigations, including numerical modelling coupling hydraulic and physico-chemical processes (e.g. Dreybrodt & Kaufmann, 2009), as well as physical models of evolving karren assemblages under artificial rainfall, gathering relevant hydraulic and hydrochemical data, would help to gain insight into the processes and factors underlying the observed morphological changes.

5.3 | Pedestal

The changes observed in the salt pedestal are in agreement with the concept whereby the umbrella effect of the capping boulder protects the upper part of the nearly vertical walls of the stem from rainfall dissolution. Erosion increases in the lower part of the stem and where the slope decreases because of two main factors: (1) these sectors are not or less shielded by the boulder; and (2) dissolutional erosion increases as the slope decreases because rainfall impinges on a proportionally smaller rock surface (i.e. higher water/surface ratio). Interestingly, no changes were observed in the position of the crown of the stem protected by the boulder. Lauritzen (2005) suggested that considerable dissolution can occur at the stem-boulder interface by condensation water and by water trickles that descend attached to the underside of the boulder by surface tension. The lack of any significant salt dissolution observed in the studied case, despite the high solubility of the rock, could be related to the prompt accumulation of impervious residual clays (dissolution residue) that can seal the top of the salt stem and prevent the access of water. As illustrates the studied example, sharp morphological changes can occur at vulnerable sites of the pedestal (e.g. grikes, holes, undercuts) reducing its persistence time or even causing its collapse.

Pedestals in limestone have been used to estimate long-term rates of surface lowering (see review in De Waele & Gutiérrez, 2022). Our high-resolution data can be used to calculate the growth rate of the pedestal height and to estimate the approximate age of the pedestal. The height of the pedestal has increased by 10–11 cm over a period of 1.96 years (715 days), yielding a growth rate of 5.1–5.6 cm/year. Considering that the salt stem was initially 45-cm high, it can be estimated that the development of the pedestal started around 8.8–8 years earlier. The calculated growth rate is around 900–500 times higher than the maximum rate (6–10 cm/kyr) reported worldwide for limestone glacial pedestals in the hyperhumid Chilean Patagonia (ca. 7000 mm/year precipitation) (André, 1996; Hobléa, Jaillet, & Maire, 2001; Maire et al., 1999), and about 250 times higher than in the coral-reef terraces (20.5 cm/ky) capped by tsunami boulders under a subtropical environment (ca. 2300 mm/year precipitation) in Kikai-jima, Ryukyu Islands, Japan, where various weathering processes may operate (Matsukura et al., 2007).

6 | CONCLUSIONS

High-resolution 3D surface models generated by close-range SfM photogrammetry are suitable for the accurate morphometric characterisation of karren and the analysis of the evolution of a variety of salt karren (solution flutes, solution bevels, pedestals) over short periods of time. To our knowledge, this is the first work that thoroughly documents the morphological evolution of real karren assemblages using time-lapse data.

The presented morphometric data indicate that solution pits and solution flutes in salt tend to have significantly larger width and much larger depth and depth-to-width ratio than those in gypsum and carbonate rocks. Rainpits display more complex shapes (i.e. irregular, elongated), often resulting from coalescence, and promptly lose their enclosed status. These differences can be ascribed to the high solubility of halite (356 g/l) and its transport-controlled dissolution kinetics, allowing the rapid growth and deepening of the pits and rills.

The investigated solution flutes in salt display rapid and complex spatial–temporal evolution patterns not consistent with the frequently advocated model of uniform slope-normal lowering (i.e. parallel retreat) that imply morphological persistence. Instead, a frequent morphological sequence is observed involving cycles of flute coalescence and flute splitting: (1) flute broadening and ridge narrowing, (2) destruction of a slim ridge with high-specific surface, (3) coalescence of adjoining rills to form a broad flute and (4) flute incision and splitting. Solution bevels show uniform slope-normal lowering and the recession of their upper edge at the expense of the rillenkarren slope. Nonetheless, differential dissolution in the bevels controlled by irregularities can locally generate enlarging inter-bevel ridges and flutes that can eventually merge with the rillenkarren slopes. Pedestals grow in height by rapid dissolutional lowering of the stem-slope junction at their foot at rates as high as 5 cm/year, until progressive or catastrophic stem narrowing led to the collapse of the stem or protecting boulder.

AUTHOR CONTRIBUTIONS

Conceptualisation: Francisco Gutiérrez and Guillermo Pérez-Villar. *Funding acquisition*: Francisco Gutiérrez. *Methodology*: Francisco Gutiérrez, Guillermo Pérez-Villar and Alfonso Benito-Calvo. *Investigation* (e.g. data collection): Francisco Gutiérrez, Guillermo Pérez-Villar, Carles Roqué and Alfonso Benito-Calvo. *Resources* (provision of data etc.): Francisco Gutiérrez and Carles Roqué. *Software* (its provision and development): Alfonso Benito-Calvo and Francisco Gutiérrez. *Supervision*: Francisco Gutiérrez. *Writing – initial draft*: Francisco Gutiérrez and Guillermo Pérez-Villar. *Writing – reviewing and editing*: Francisco Gutiérrez, Guillermo Pérez-Villar, Alfonso Benito-Calvo and Carles Roqué.

ACKNOWLEDGEMENTS

This work has been developed by DIAPERNO Project (PID2021-123189NB-I00) funded by the Spanish Government (Ministerio de Ciencia e Innovación). Authors are grateful to Mr. Ferrán Climent (Director of Catalunya Central Geoparc) for logistic support. GPV has a pre-doctoral contract (PRE2022-101600) co-financed by the Spanish Government (MCIN/AEI/10.13039/501100011033) and the European Social Fund (FSE+). GPV and FG belong to the IUCA research group of the Aragón Government. Authors are very grateful to two anonymous reviewers for their insightful comments.

DATA AVAILABILITY STATEMENT

Data are available upon request.

ORCID

Guillermo Pérez-Villar https://orcid.org/0000-0002-6607-2395

REFERENCES

André, M.F. (1996) Vitesses de dissolution aréolaire postglaciaire dans les karsts polaires et haut-alpins. De l'arctique scandinave aux Alps de Nouvelle-Guinée. *Revue D'analyse Spatiale Quantitative et appliquée*, 38(39), 99–107.

Bögli, A. (1960) Kalklösung und Karrenbildung. *Zeitschrift Für Geomorphologie*, 2, 4–21.

Bögli, A. (1961) Karrentische, ein Beitrag zur Karstmorphologie. *Zeitschrift Für Geomorphologie*, NF, 5, 185–193.

Bruthans, J., Filippi, M., Asadi, N., Zare, M., Šlechta, S. & Churáčková, Z. (2009) Surficial deposits on salt diapirs (Zagros Mountains and Persian Gulf Platform, Iran): characterization, evolution, erosion and the influence on landscape morphology. *Geomorphology*, 107(3–4), 195–209. Available from: https://doi.org/10.1016/j.geomorph.2008.12.006

Cardona, F. & Viver, J. (2002) *Sota la sal de Cardona*. Barcelona: Espeleo Club de Gracia, p. 128.

Crowther, J. (1998) New methodologies for investigating rillenkarren cross-sections: a case study at Lluc, Mallorca. *Earth Surface Processes and Landforms*, 23(4), 333–344. Available from: https://doi.org/10.1002/(SICI)1096-9837(199804)23:4<>3.0.CO;2-Z

De Waele, J. & Gutiérrez, F. (2022) *Karst hydrogeology, geomorphology and caves*. Chichester, West Sussex: John Wiley & Sons.

Dreybrodt, W., and Kaufmann, G. (2009) Physics and chemistry of dissolution on subaerialy exposed soluble rocks by flowing water films. In: Ginés, À., Knez, M., Slabe, T., and Dreybrodt, W. (Eds.) *Karst rock features. Karren sculpturing* (9). Ljubljana: Zalozba ZRC. pp. 25–36.

Dunkerley, D. (1979) The morphology and development of rillenkarren. *Zeitschrift Für Geomorphologie*, 23(3), 332–348.

Fiol, L., Fornós, J.J. & Ginés, A. (1996) Effects of biokarstic processes on the development of solutional rillenkarren in limestone rocks. *Earth Surface Processes and Landforms*, 21(5), 447–452. Available from: https://doi.org/10.1002/(SICI)1096-9837(199605)21:5<447::AID-ESP607>3.0.CO;2-X

Ford, D.C. & Lundberg, J. (1987) A review of dissolutional rills in limestone and other soluble rocks. *Catena Supplement*, 8, 119–140.

Ginés, A. 1996. An environmental approach to the typology of karren landform assemblages in a Mediterranean midmountain karst: the Serra de Tramuntana, Mallorca, Spain. In Karren landforms: Proceedings of the International Symposium on Karren Landforms, 19-24th of September 1995, 163–176. Universitat de les Illes Balears.

Ginés, A. (1998) *Dades morfomètriques sobre les estries de lapiaz dels Alps calcaris suïssos i la seva comparació amb les estries de la Serra de Tramuntana*. Endins: publicació d'espeleologia, pp. 109–118.

Ginés A. (1999) Morfología kárstica y vegetación en la Serra de Tramuntana. Una aproximación ecológica. Unpublished Ph. D. Thesis, Departament de Biología Ambiental, Universitat de les Illes Balears

Ginés, A., Knez, M., Slabe, T. & Dreybrodt, W. (Eds). (2009) *Karst Rock Features. Karren Sculpturing*, Vol. 9. Ljubljana: Založba ZRC.

Ginés, A. & Lundberg, J. (2009) Rainpits: An outline of their characteristics and genesis. In: Ginés, À., Knez, M., Slabe, T. & Dreybrodt, W. (Eds.) *Karst rock features. Karren Sculpturing*, Vol. 9. Ljubljana: Zalozba ZRC, pp. 169–184.

Glew, J.R. & Ford, D.C. (1980) A simulation study of the development of rillenkarren. *Earth Surface Processes*, 5(1), 25–36. Available from: https://doi.org/10.1002/esp.3760050104

Hobléa, F., Jaillet, S. & Maire, R. (2001) Erosion et ruissellement sur karst nu: les îles subpolaires de la Patagonie chilienne (Magallanes, Chili). *Karstologia: Revue De Karstologie et De Spéléologie Physique*, 38(1), 13–18. Available from: https://doi.org/10.3406/karst.2001.2480

Jackson, M.P.A. and Hudec, M.R. (2017) *Salt tectonics: principles and practice*. Cambridge: Cambridge University Press, https://doi.org/10.1017/9781139003988

James, M.R., Chandler, J.H., Eltner, A., Fraser, C., Miller, P.E., Mills, J.P., et al. (2019) Guidelines on the use of structure-from-motion photogrammetry in geomorphic research. *Earth Surface Processes and Landforms*, 44(10), 2081–2084. Available from: https://doi.org/10.1002/esp.4637

Lauritzen S. E. (2005) A simple growth model for allogenic pedestals in glaciated karst. In *14th International Congress of Speleology*. Athen-Kalamos 21-28th August, O-52

Lucha, P., Cardona, F., Gutiérrez, F. & Guerrero, J. (2008) Natural and human-induced dissolution and subsidence processes in the salt outcrop of the Cardona Diapir (NE Spain). *Environmental Geology*, 53(5), 1023–1035. Available from: https://doi.org/10.1007/s00254-007-0729-3

Lundberg J. (1977) The geomorphology of Chillagoe limestones: variations with lithology. Unpublished M. Sc. thesis, Australian National University, Canberra

Lundberg, J. (2013) Microsculpturing of solutional rocky landforms. In: Frumkin, A. (Ed.) *Treatise of geomorphology: karst geomorphology*, Vol. 6. Amsterdam: Elsevier, pp. 121–138.

Lundberg, J. & Ginés, À. (2009) Rillenkarren. In: Ginés, À., Knez, M., Slabe, T. & Dreybrodt, W. (Eds.) *Karst rock features. Karren sculpturing*, Vol. 9. Ljubljana: Zalozba ZRC, pp. 185–210.

Macaluso, T. & Sauro, U. (1996) Weathering crust and karren on exposed gypsum surfaces. *International Journal of Speleology*, 25(3), 9.

Maire, R., l'équipe Ultima Esperanza, Pernette, J.F. & Fage, L.H. (1999) Les 'glaciers de marbre' de Patagonie, Chili: Un karst subpolaireocéanique de la zone australe. *Karstologia*, 33, 25–40.

Matsukura, Y., Maekado, A., Aoki, H., Kogure, T. & Kitano, Y. (2007) Surface lowering rates of uplifted limestone terraces estimated from the height of pedestals on a subtropical island of Japan. *Earth Surface Processes and Landforms*, 32(7), 1110–1115. Available from: https://doi.org/10.1002/esp.1510

Mottershead, D. (1996) Some morphological properties of solution flutes (Rillenkarren) at Lluc, Mallorca. In *Karren landforms: Proceedings of the International Symposium on Karren Landforms*. Universitat de les Illes Balears 19-24th of September, 225-238.

Mottershead, D. & Lucas, G. (2001) Field testing of Glew and Ford's model of solution flute evolution. *Earth Surface Processes and Landforms*, 26(8), 839–846. Available from: https://doi.org/10.1002/esp.229

Mottershead, D. & Lucas, G. (2004) The role of mechanical and biotic processes in solution flute development. In: Smith, B.J. & Turkington, A. (Eds.) *Stone decay: its causes and controls*. Abingdon, Oxon and New York: Donhead Publishing Ltd, pp. 273–291.

Mottershead, D.N., Moses, C.A. & Lucas, G.R. (2000) Lithological control of solution flute from: a comparative study. *Zeitschrift Für Geomorphologie*, 44(4), 491–512.

Palmeri, V., Madonia, G. & Ferro, V. (2020) Capturing gypsum rillenkarren morphometry by a 3D-photo reconstruction (3D-PR) technique. *Geomorphology*, 351, 106980. Available from: https://doi.org/10.1016/j.geomorph.2019.106980

Pérez-Villar, G., Gutiérrez, F., Bausilio, G. & Di Martire, D. (2025) Integrating DInSAR and detailed mapping for characterizing ground displacement in the Cardona salt extrusion related to diapiric uplift, dissolutional lowering, landsliding and sinkholes. *Engineering Geology*, 352, 108068. Available from: https://doi.org/10.1016/j.enggeo.2025.108068

Pérez-Villar, G., Gutiérrez, F., Zarroca, M., Roqué, C., Benito-Calvo, A. & Menció, A. (2024) Late Quaternary morpho-stratigraphic record of diapir rise in the Cardona salt extrusion, NE Spain. Halokinetic sequences, raised terraces and uplift rates. *Quaternary Science Reviews*, 324, 108462. Available from: https://doi.org/10.1016/j.quascirev.2023.108462

Pueyo J.J. (1975) Estudio petrológico y geoquímica de los yacimientos potásicos de Cardona, Suria, Sallent y Balsareny (Barcelona, España). Unpublished PhD Thesis, Universidad de Barcelona.

Riba, O., Ramírez del Pozo, J. and Maldonado, A. (1975) Mapa Geológico de España, 1:50.000. Cardona (330). *IGME*, Madrid.

Riba, O., Reguant, S. & Villena, J. (1983) Ensayo de síntesis estatigráfica y evolutiva de la cuenca terciaria del Ebro. In: Ríos, J.M. (Ed.) *Geología de España*, Vol. 2. IGME, Madrid: Libro Jubilar IGME, pp. 131–159.

Rosell, L. & Pueyo, J.J. (1997) Second marine evaporitic phase in the South Pyrenean Foredee: The Priabonian Potash Basin (Late Eocene: Autochthonous–allochthobous Zone). In: Busson, G. & Schreiber, C. (Eds.) *Sedimentary deposition in rift and foreland basins in France and Spain*. New York: Columbia University Press, pp. 358–387.

Sans, M. (2003) From thrust tectonics to diapirism. The role of evaporites in the kinematic evolution of the eastern South Pyrenean front. *Geologica Acta*, 1, 239–259.

Sans, M. & Verges, J. (1995) Fold development related to contractional salt tectonics: Southeastern Pyrenean Thrust Front, Spain. In: Jackson, M.P.A., Roberts, D.G. & Snelson, S. (Eds.) *Salt tectonics: a global perspective*, Vol. 65. AAPG Memoir, pp. 369–378. Available from: https://doi.org/10.1306/M65604

Slabe, T., Hada, A. & Knez, M. (2016) Laboratory modeling of karst phenomena and their rock relief on plaster: subsoil karren, rain flutes karren and caves. *Acta Carsologica*, 45(2), 187–204. Available from: https://doi.org/10.3986/ac.v45i2.4623

Smith, B.J. (1987) An integrated approach to the weathering of limestone in an arid area and its role in landscape evolution: a case study from Southeast Morocco. In: Gardiner, V. (Ed.) *International geomorphologyy*, pp. 637–657. Chichester: Wiley.

Stenson, R.E. & Ford, D.C. (1993) Rillenkarren on gypsum in Nova Scotia. *Géographie Physique et Quaternaire*, 47(2), 239–243. Available from: https://doi.org/10.7202/032951ar

Talbot, C.J. & Jackson, M.P.A. (1987) Internal kinematics of salt diapirs. *AAPG Bulletin*, 71(9), 1068–1093.

Talbot, C.J. & Pohjola, V. (2009) Subaerial salt extrusions in Iran as analogues of ice sheets, streams and glaciers. *Earth-Science Reviews*, 97(1-4), 155–183. Available from: https://doi.org/10.1016/j.earscirev.2009.09.004

Williams, P.W. (2011) Karst in UNESCO world heritage sites. In: van Beynen, P. (Ed.) *Karst Management*, 459–480. Dordrecht: Springer. Available from: https://doi.org/10.1007/978-94-007-1207-2_21

Zarei, M., Raeisi, E. & Talbot, C.J. (2012) Karst development on a mobile substrate: Konarsiah salt extrusion, Iran. *Geological Magazine*, 149(3), 412–422.

Zhang, D. (1994) Distribution of Tibetan karren and their morphogenetic analysis. *Carsologica Sinica*, 13(3), 270–280.

How to cite this article: Pérez-Villar, G., Gutiérrez, F., Benito-Calvo, A. & Roqué, C. (2025) Morphometry and spatio-temporal evolution of salt karren. *Earth Surface Processes and Landforms*, 50(8), e70119. Available from: https://doi.org/10.1002/esp.70119